Materials Advances

ROYAL SOCIETY OF CHEMISTRY

PAPER

View Article Online
View Journal | View Issue

Cite this: *Mater. Adv.*, 2024, 5, 8199

Li_2MnCl_4 single crystal: a new candidate for a red-emitting neutron scintillator†

Vojtěch Vaněček, ‡*[ab] Robert Král,[a] Kateřina Křehlíková,[a] Romana Kučerková,[a] Vladimir Babin,[a] Petra Zemenová,[a] Jan Rohlíček,[a] Zuzana Málková,[a] Terézia Jurkovičová[a] and Martin Nikl[a]

Received 9th July 2024,
Accepted 12th September 2024

DOI: 10.1039/d4ma00697f

rsc.li/materials-advances

A novel red-emitting scintillator Li_2MnCl_4 is proposed as a candidate for thermal neutron detection. It features high Li content, low density, a low effective atomic number, and emission in the red-NIR region. These characteristics make it an interesting candidate for long-distance neutron detection in harsh environments *e.g.* decommissioning of nuclear power plants. The absorption is thoroughly investigated in the scope of the Tanabe–Sugano diagram. The luminescence mechanism in undoped Li_2MnCl_4 is studied in depth using steady-state and time-resolved photoluminescence. Doping with Eu^{2+} and Ce^{3+} is introduced as a trial to improve the scintillation efficiency. We show that in the Eu^{2+} and Ce^{3+} doped Li_2MnCl_4 the luminescence mechanism involves energy transfer from the dopants to Mn^{2+}, and propose the local lattice distortion around the dopant and possible charge compensation mechanisms.

Introduction

Detection and spectroscopy of neutrons is crucial for applications ranging from large spallation sources[1] to nuclear non-proliferation.[2] The ^{3}He shortage[3] limits the future use of ^{3}He proportional counters which are currently the most commonly used neutron detectors. The main source of ^{3}He is radioactive decay for tritium. After World War 2 both USA and USSR kept large reserves of tritium for military uses. Therefore, an abundance of ^{3}He was available as a byproduct of nuclear warfare. However, after the end of the Cold War, both the USA and USSR significantly lowered their tritium reserves and, as a result, production of ^{3}He drastically dropped. Decreasing production of ^{3}He together with increasing demand results in the inevitable depletion of ^{3}He reserves and a steep increase in the price, which is becoming unaffordable for non-USA industry. Therefore, it is necessary to develop novel neutron detectors that would be able to replace ^{3}He proportional counters in some applications. One of the fields where not only the replacement of ^{3}He detectors but also advances in neutron detection are necessary are neutron scattering experiments at large spallation sources[4] and decommissioning of nuclear power plants.[5]

This work reports on the optical, luminescence and scintillation characteristics of undoped and Eu^{2+} and Ce^{3+} doped Li_2MnCl_4 single crystals. These materials are an interesting candidate for thermal neutron detection due to the high content of Li, low density, and a low effective atomic number. This combination of material properties is a prerequisite for an effective n/γ discrimination in mixed radiation fluxes which is a necessity in many applications. Moreover, emission in the red-infrared spectral region is favourable for pairing with modern semiconductor photodetectors.

Experimental

As starting materials powders of LiCl (99+%, Merck) and $MnCl_2$ (97%, Thermo Fisher Scientific), EuS (99.99%, Changsha Easchem), and Ce_2S_3 (99.99%, Changsha Easchem) were used. Both LiCl and $MnCl_2$ were further purified by the introduction of halogenating agents (HCl and $COCl_2$) into the melt and successive zone refining (>20 passes of the melted zone) according to ref. 6 and 7. Material from the middle section of the zone refined ingot was selected for crystal growth for both LiCl and $MnCl_2$. In the case of LiCl, the zone refined ingot was transparent and colourless. In the case of $MnCl_2$, the zone refined ingot was deep red and formed flakes upon mechanical stress. Such behaviour is typical for divalent halides with layered crystal structures *e.g.* $MgCl_2$, $CdCl_2$, $CdBr_2$, CdI_2, or PbI_2. Stoichiometric amounts of purified LiCl and $MnCl_2$ (and EuS or Ce_2S_3) were weighed into fused silica ampoules and sealed under vacuum using an oxygen–hydrogen torch.

[a] *Institute of Physics of the Czech Academy of Sciences, Cukrovarnicka 10/112, Prague, 16200, Czech Republic. E-mail: vanecekv@fzu.cz*
[b] *IMR, Tohoku University, 2-1-1, Katahira, Aoba-ku, Sendai, Miyagi, 980-8577, Japan*

† Electronic supplementary information (ESI) available. See DOI: https://doi.org/10.1039/d4ma00697f

‡ JSPS International research fellow.

The crystals were grown using a single zone inductively heated vertical Bridgman furnace as described in ref. 8. During the entire growth, the furnace was continuously evacuated using a rotary vane pump to minimize heat transfer *via* convection and therefore prevent the unwanted chimney effect. This results in a steeper temperature gradient and a more stable temperature profile. The pressure was maintained at approx. 1 Pa during the entire growth. The growth rate was 0.6 mm h^{-1}, and the cooling time was 40 hours.

For the X-ray powder diffraction (XRPD) analysis, the crystal samples were powdered in an alumina mortar and pestle and placed in the ∅ 0.5 mm borosilicate-glass capillary in an atmosphere-controlled glovebox (concentration of O_2 and H_2O < 1 ppm). The capillary was sealed with rubber to prevent the degradation of the sample during the measurement. Powder diffraction data were collected using the Debye–Scherrer transmission configuration on an Empyrean, PANalytical powder diffractometer ($\lambda_{Cu,K\alpha}$ = 1.54184 Å) that was equipped with a focusing mirror, a capillary holder, and a PIXcel3D detector.

Radioluminescence (RL) spectra, measured in the spectral range of 190–800 nm at room temperature, were obtained using a custom-made spectrofluorometer 5000 M, Horiba Jobin Yvon. Tungsten-cathode X-ray tube Seifert was used as the excitation source (at 40 kV, 15 mA). The detection part of the set-up consisted of a single grating monochromator and photon-counting detector TBX-04, Horiba, or an Ocean Optical CCD detector (based on the spectral range). The measured spectra were corrected for the spectral response of the setup. Photoluminescence decays were measured at 5000 M using multichannel scaling and time-correlated single photon counting techniques under the excitation of a microsecond flashlamp (μs-ms time scale) and nanosecond nanoLED (sub-μs time scale) excitation sources, respectively. To extract the true decay times, the measured decays were fitted by a sum of exponential terms convoluted with the instrumental response to the excitation pulse.

Non-isothermal DSC was carried out using the Setaram Themys 24 apparatus. The nominal charge of 65 mg of the powder Li_2MnCl_4 material was sealed in a quartz ampule under vacuum. Sealing the Li_2MnCl_4 powder under vacuum in a small quartz ampule enabled the simulation and monitoring of heat conditions similar to those present during the Li_2MnCl_4 crystal growth by the Bridgman method. All DSC experiments were carried out with a heating rate of 10 K min^{-1} in the temperature range of 25–650 °C and with an empty sealed quartz ampule in alumina crucible as a reference. The DSC apparatus was calibrated in the temperature range of 25–1300 °C using the following standards (In, Sn, Zn, Al, Ag, and Au). The standard deviation of performed calibrations was in the range of ±1 K. Processing of the obtained data was carried out using the Calisto Processing software.

The ratio of lithium and manganese in the Li_2MnCl_4 monocrystal samples was determined by flame atomic absorption spectrometry (FAAS). Samples with weights ranging from 5.8 mg to 8.5 mg were slowly heated in 3 mL HCl (1 : 1) (HCl purchased from P-Lab, Czech Republic) and fully decomposed. When the temperature of the samples decreased, they were transferred into 100 mL volumetric flasks and 7 mL of KCl (with a concentration of 6 g of KCl in 100 mL) was added to decrease the ionization of lithium. Finally, distilled water was added to the volume of 100 mL in a volumetric flask. The calibration curve was prepared by combining both elements using lithium and manganese standard solutions in the same way as sample solutions. A Varian AA240 FAAS (Varian Inc., Palo Alto, California, US) equipped with Li and Mn hollow cathodes (Varian Inc., Palo Alto, California, US) was used for the elemental concentration determination. The instrument conditions, such as wavelengths (670.8 nm for Li and 403.1 nm for Mn, respectively), 1.0 nm slit width, 10 cm burner, and the air-acetylene flame were employed according to the standard recommendations for both elements.[9] All the solutions were manually injected. The concentration of Li and Mn were determined from the concentration curves and subsequently, the ratio of Li and Mn in the samples was calculated. The relative standard deviation of determination was 2%.

Due to the hygroscopic nature of used materials, great care was taken to prevent degradation *via* reaction with moisture. Whenever possible handling of all hygroscopic materials (starting materials, zone refined ingots, grown crystals, *etc.*) was performed in the atmosphere-controlled glovebox using dry nitrogen (concentration of O_2 and H_2O < 1 ppm) as the protective atmosphere. When manipulation outside of the glovebox was necessary the materials were placed inside fused silica ampoules closed with a vacuum-tight valve or seal. However, due to technical limitations, most of the optical characterization was performed under ambient conditions. Whenever possible samples were immersed in/coated by luminescence-free immersion oil (Fluka) to suppress the degradation process.

Results and discussion

The crystal growth under optimized conditions resulted in homogeneous boules with no macroscopic defects. The undoped crystal is transparent and pink in colour while both Eu^{2+} and Ce^{3+} doped samples are deep red, which limits their transparency (see Fig. 1A–C). Cut and polished disc-like samples with dimensions of ∅ 7 × 1.5 mm were prepared for all three crystals (see Fig. 1D–F).

The XRD measurement was performed on the powder Li_2MnCl_4 (LMC) samples (selected from the middle of the as-grown crystal) confirming the presence of the Li_2MnCl_4 phase (see Fig. 2). Li_2MnCl_4 exhibits a spinel crystal structure (space group $Fd\bar{3}m$, no. 227, phase prototype $MgAl_2O_4$). Using a general spinel formula:

$$(A_{1-x}B_x)^{tet}[A_{x/2}B_{1-x/2}]_2^{oct}X_4,$$

where elements in round brackets occupy tetrahedral lattice sites and elements in square brackets occupy octahedral lattice sites, x = 0 represents regular spinel, and x = 1 an inverse spinel structure a Li_2MnCl_4 can be represented as:

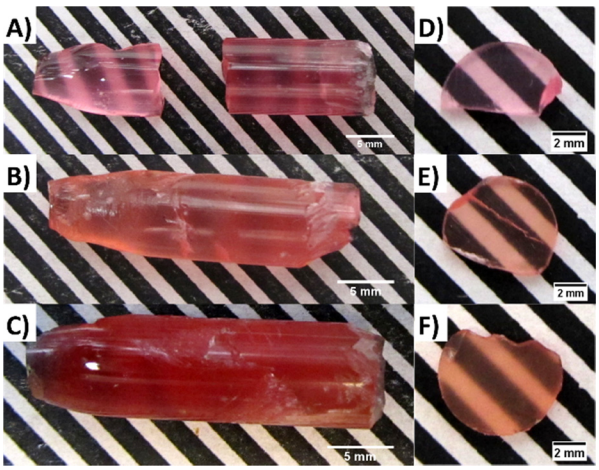

Fig. 1 Photos of as the grown crystals of (A–C) and samples prepared for optical characterization (D–F) of undoped Li_2MnCl_4 (A) and (D), $Li_2MnCl_4:Eu^{2+}$ (B) and (E), and $Li_2MnCl_4:Ce^{3+}$ (C) and (F) respectively.

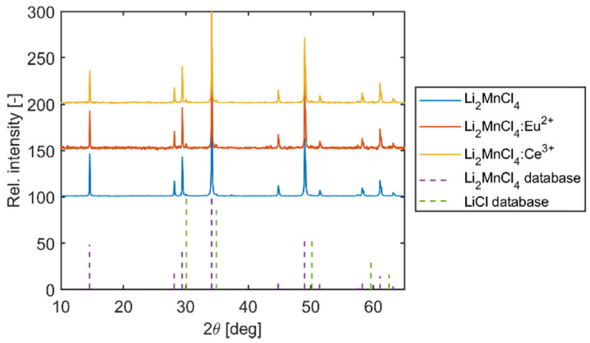

Fig. 2 X-ray powder diffraction of samples prepared from all three Li_2MnCl_4 crystals. The database records for Li_2MnCl_4 (ICSD PDF no. 01-070-0935) and LiCl (ICSD PDF no. 00-004-0664) are shown in dashed lines.

$$(Li)^{tet}[Li_{0.5}Mn_{0.5}]_2^{oct}Cl_4,$$

where A = Mn^{2+}, B = Li^+, X = Cl^-, and $x = 1$. Therefore, Li_2MnCl_4 is a fully inverse chloride spinel as reported by Lutz and Schneider.[10] Very weak reflections corresponding to LiCl were identified in the diffractograms of all three Li_2MnCl_4 crystals (see Fig. 2). It can be observed mainly through the two strongest reflections at 30.1° and 34.9° corresponding to the (1 1 1) and (2 0 0) lattice planes of cubic LiCl, respectively. The presence of LiCl is probably due to a slight off-stoichiometry and will be subject to future crystal growth optimization. Based on the ionic size and charge it is expected for both Eu^{2+} and Ce^{3+} to replace Mn^{2+} in the octahedral coordination (for details see section "Luminescence mechanism in doped samples").

To further elucidate the composition of the grown crystals, the Li : Mn molar ratio was measured using flame atomic absorption spectroscopy (FAAS). Samples from the start (conic part) and the end (cylindrical part) of the grown undoped crystals were analysed. The FAAS results revealed that in the samples taken from the start (first-to-freeze) and the end (last-to-freeze) of the as-grown undoped Li_2MnCl_4 the atomic ratio of Li : Mn is close to the ideal stoichiometry (see Table 1). However, the results point toward the slight depletion of Li towards the end of the growth. This could be caused by high lithium mobility in Li_2MnCl_4 crystals. The ionic mobility of Li^+ in several chloride spinels with composition Li_2BX_4 where B = Mn, Cd, Mg, and Fe and X = Cl or Br[11–13] was investigated in the 1980s for application as solid Li electrolytes. The temperature-dependent conductivity measurements showed that the conductivity of the melt is only twice as high as the conductivity of the solid sample just below the melting point.[12] Such a high ionic conductivity could result in significant Li^+ migration in the solid phase during crystal growth.

Table 1 Results of the flame atomic absorption spectrometry. Samples labelled "s" were taken from the first-to-freeze section and samples labelled "e" were selected from the last-to-freeze section of the as-grown undoped Li_2MnCl_4 crystal

Sample	m [mg]	m(Mn) [mg]	m(Li) [mg]	Li : Mn
s1	8.1	2.12	0.54	2.02 : 1.00
s2	6.5	1.71	0.42	1.95 : 1.00
e1	8.5	2.2	0.54	1.95 : 1.00
e2	6.8	1.78	0.43	1.91 : 1.00

The DSC measurement revealed two endothermic effects at onset temperatures of 442 ± 3 °C and 573 ± 1 °C (see Fig. S1a, ESI†) on the heating curve and 459 ± 1 °C and 570 ± 1 °C (see Fig. S1b, ESI†) on the cooling curve. Both effects were reproducibly detected in four heating–cooling cycles. Therefore, it is assumed that the effects are reversible. The endothermic effect at around 450 °C was reported by several authors,[11,14,15] Lutz *et al.*[15] ascribed this effect to the phase transition from spinel to the defect rock salt structure. Such phase transition might result in residual stress in the as-grown crystals. However, no cracking of the crystals during processing was observed. The second effect at 573 ± 1 °C is ascribed to congruent melting of the high-temperature Li_2MnCl_4 phase and corresponds well with the values reported in the literature.[14,15] Interestingly, undercooling of only 3 °C was observed. This effect is probably caused by the low volume-to-surface ratio of the sample and the large contact surface of the melt with the quartz ampule which serves as a heterogeneous nucleation centre.

Absorption spectra

The measurement of absorption was complicated due to the continuous degradation of the sample during measurement. The degradation results in the formation of a structured surface which leads to a strong scattering of light. Such scattering manifests as a diffuse background which is non-linearly increasing towards shorter wavelengths. Therefore, reliable estimation of the optical band gap from the absorption edge was impossible. This effect is also responsible for the atypical shape of the absorption spectra at longer wavelengths. Since the measurements proceeded from the long wavelength side of the spectrum the beginning of the measurement is heavily affected by ongoing degradation of the sample. Nevertheless, distinct absorption bands could be observed for all three samples (see Fig. 3).

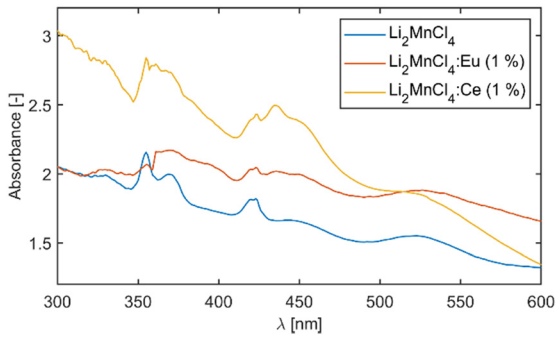

Fig. 3 Absorption spectra of the Li_2MnCl_4 samples.

The absorption spectrum of the undoped sample was analysed in the scope of the Tanabe–Sugano diagram. The positions of the absorption bands were extracted *via* fitting. To suppress the influence of the diffuse background on the position of the absorption bands the first derivative of the absorption spectrum was fitted assuming the Gaussian shape of the absorption bands (see Fig. S2, ESI†). The use of six Gaussian components resulted in a satisfactory fit in the range from 2 eV (620 nm) to 4 eV (310 nm). The vast majority of the experimental points are within 95% prediction bounds of the used model. Although the peak centred around 3.36 eV (370 nm) is quite asymmetric which results in lower accuracy of the fit, the goodness of fit is still satisfactory. The asymmetric shape of the absorption band might be caused by the superposition of two bands. For illustration, Fig. S3 (ESI†) shows a comparison between the measured absorption spectra and the normalized spectrum reconstructed from the first derivative fitting. The positions of all six bands were compared to the d^5 Tanabe–Sugano diagram. The best agreement (least squares) was at $D_q/B = 9.1$ which corresponds to a value of Racah parameter $B = 725 \pm 7$ cm^{-1}. The decrease of B compared to free ion value $B_{free}(Mn^{2+}) = 860$ cm^{-1} (ref. 16) is due to the nephelauxetic effect. The value B/B_{free} of 0.84 is reasonable compared to 0.95 for MnF_2, 0.90 for NaCl:Mn^{2+},[16] or 0.88 for $CaCl_2$:Mn^{2+}.[17]

Fig. 4 depicts the absorption spectra of undoped Li_2MnCl_4 with an indication of band positions and their assignment based on the d^5 Tanabe–Sugano diagram. The double peak with maxima around 420 nm is due to coinciding $^6A_{1g}$ (^6S) → $^4A_{1g}$ (^4G) and $^6A_{1g}$ (^6S) → ^4E_g (^4G) transitions and no direct

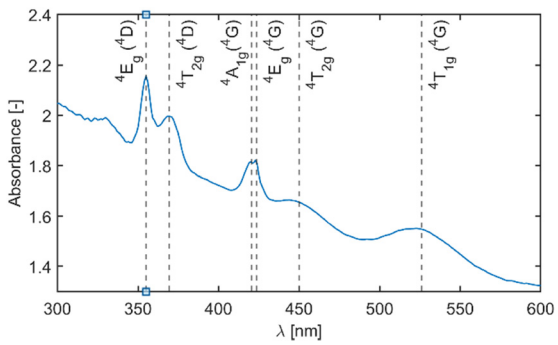

Fig. 4 Absorption spectra of undoped Li_2MnCl_4 with indication of band positions and their assignment based on the d^5 Tanabe–Sugano diagram.

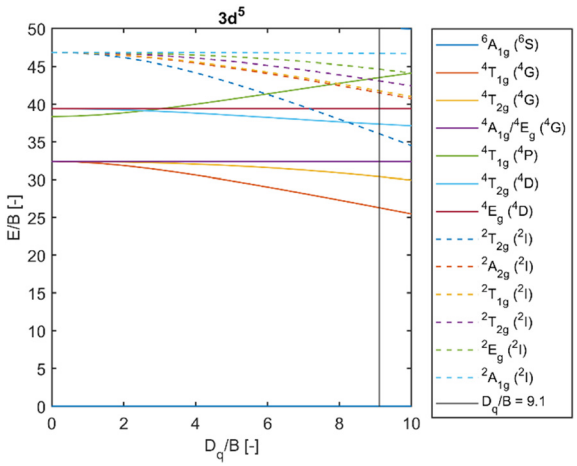

Fig. 5 Section of the d^5 Tanabe–Sugano diagram with indication of the D_q/B = 9.1. Doublet levels are in dashed lines. Reproduced from ref. 18.

assignment between the two can be currently made. The mean maxima position was used for the calculation of the B Racah parameter.

Fig. 5 depicts a section of the d^5 Tanabe–Sugano diagram[18] with an indication of the D_q/B = 9.1. Transitions from the ground sextet to all quartets can be observed in the absorption spectra. The only exception is transition $^6A_{1g}$ (^6S) → $^4T_{1g}$ (^4P) which should be positioned around 320 nm. The position roughly correlates with a weak deformed peak at 330 nm. Therefore, we assume that the absorption band centred at 330 nm corresponds to the $^6A_{1g}$ (^6S) → $^4T_{1g}$ (^4P) transition. The PLE measurements are in agreement with this assumption (see Fig. 6 below).

Transitions from the ground sextet to the doublet levels (^2I) exhibit very low oscillator strength due to high difference in spin number, *i.e.* strongly spin/forbidden transitions. Therefore, these transitions should not be observable. However, the overlap of the $^6A_{1g}$ (^6S) → $^4T_{2g}$ (^4D) and $^6A_{1g}$ (^6S) → $^2T_{2g}$ (^2I) transitions might be the reason for the asymmetry of the $^6A_{1g}$ (^6S) → $^4T_{2g}$ absorption band. The ascription is consistent with the available literature.[19–22]

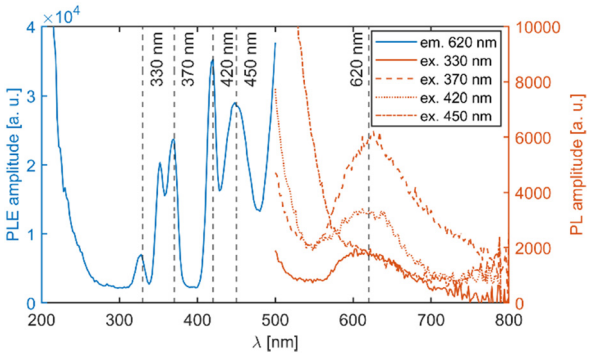

Fig. 6 PLE and PL spectra of the undoped Li_2MnCl_4 sample. The excitation and emission wavelengths are indicated by dashed lines. The high intensity at around 200 and 500 nm is due to overcorrection and light scattering respectively.

Photoluminescence spectra

Li_2MnCl_4. The PL spectra (see Fig. 6) show a broad band centred around 620 nm for all excitation wavelengths. This band can be ascribed to the $^4T_{1g}$ (^4G) → $^6A_{1g}$ (^6S) transition. Excitation to the higher quartet levels is followed by the non-radiative relaxation to the lowest excited level ($^4T_{1g}$) and radiative transition to the ground level ($^6A_{1g}$). Broad emission is due to different slopes of the $^4T_{1g}$ (^4G) and the $^6A_{1g}$ (^6S) levels at D_q/B = 9.1 and the sensitivity of the $^4T_{1g}$ (^4G) excited state to the crystal field. Increasing intensity towards 500 nm is due to excitation light scattering. The PLE spectra monitored at 620 nm are in good agreement with the absorption spectra (see Fig. S4, ESI†). The excitation band centred around 330 nm is much more pronounced compared to the absorption spectra which corroborates with assignment to the $^6A_{1g}$ (^6S) → $^4T_{1g}$ (^4P) transition.

Li_2MnCl_4:Eu^{2+}. In PL of the Eu^{2+} doped Li_2MnCl_4 sample (see Fig. 7) a narrow band centred at 405 nm is observed. Based on the shape and position of the band[23] it is ascribed to 5d → 4f emission of Eu^{2+}. Interestingly, the red emission band extends much further into the NIR (outside of the sensitive region of used PMT) compared to the undoped sample. The origin of this effect is discussed in the "Luminescence mechanism in doped samples" section below. Moreover, there is a partial overlap between the emission of Eu^{2+} and the excitation of the host matrix (λ_{em} = 670 nm). Such overlap could enable energy transfer from Eu^{2+} to Mn^{2+} further facilitated by their close proximity in the crystal structure. Indeed, the energy transfer from Eu^{2+} to Mn^{2+} can be seen in the PL spectrum excited at 340 nm. Based on the comparison of PLE spectra of undoped Li_2MnCl_4 (see Fig. 6, λ_{em} = 620 nm) and Eu^{2+} in Li_2MnCl_4:Eu (see Fig. 7, λ_{em} = 410 nm), Eu^{2+} is selectively excited at 340 nm. However, the PL spectrum of Li_2MnCl_4:Eu excited at 340 nm clearly shows both Eu^{2+} and Mn^{2+} emissions (see Fig. 7). The energy transfer from Eu^{2+} to Mn^{2+} also gives rise to the additional excitation bands at <320 nm in the PLE spectrum of Mn^{2+} (λ_{em} = 670 nm). The PLE spectrum for λ_{em} = 770 nm has the same features as the PLE spectrum for λ_{em} = 670, but with much lower intensity (see Fig. S5 for detail, ESI†). Nevertheless, even

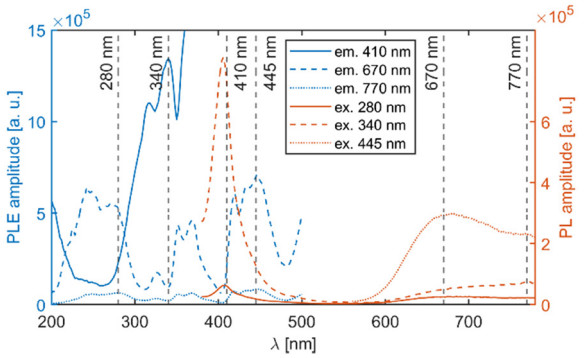

Fig. 7 PLE and PL spectra of the Li_2MnCl_4:Eu^{2+} (1%) sample. The excitation and emission wavelengths are indicated by dashed lines. The high intensity at around 200 nm is due to overcorrection.

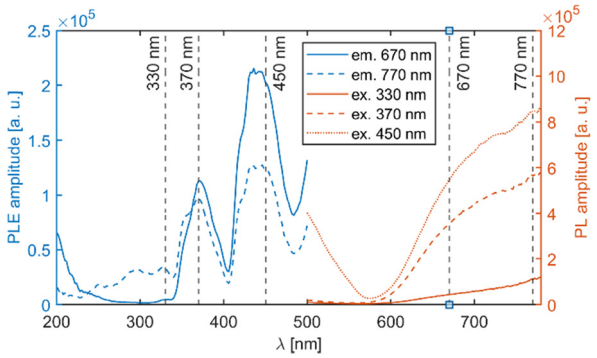

Fig. 8 PLE and PL spectra of the Li_2MnCl_4:Ce^{3+} (1%) sample. The excitation and emission wavelengths are indicated by dashed lines. The high intensity at around 200 and 500 nm is due to overcorrection and light scattering respectively.

direct Mn^{2+} excitation at 445 nm ($^6A_{1g}$ (^6S) → $^4T_{2g}$ (^4D)) in Li_2MnCl_4:Eu results in a much broader emission band compared to undoped Li_2MnCl_4.

Li_2MnCl_4:Ce^{3+}. The emission band which could be ascribed to 5d → 4f emission of Ce^{3+} was not observed in the PL spectra of Li_2MnCl_4:Ce. This is probably due to efficient energy transfer from Ce^{3+} to Mn^{2+}. Based on the linear relationship between the position of 5d → 4f emission of Eu^{2+} and Ce^{3+} (see Dorenbos[24]) and the position of the lowest 4f–5d_1 absorption bands of Eu^{2+} and Ce^{3+} in chloride hosts[23,25] the 5d → 4f emission of Ce^{3+} in Li_2MnCl_4 should be centred at around 320–340 nm which would result in strong overlap with the $^6A_{1g}$ (^6S) → $^4T_{1g}$ (^4P) absorption band of Mn^{2+} thus enabling an efficient Ce^{3+} → Mn^{2+} energy transfer further intensified by about 10× higher oscillator strength of the 4f–5d_1 transition of Ce^{3+} compared to that of Eu^{2+}. Similarly to the Li_2MnCl_4:Eu^{2+}, Ce^{3+} doping gives rise to a broad emission band (see Fig. 8) extending from red to NIR (for details see the "Luminescence mechanism in doped samples" section below). PL spectra excited at different wavelengths (330, 370, and 450 nm) have very similar band shapes, but differ in intensity in accordance with the intensity of respective PLE bands. However, in contrast to Eu^{2+} doping, the PL band in the Ce^{3+} doped sample does not exhibit a maximum in the measured range. Ce^{3+} doping also results in the appearance of excitation bands at <320 nm which are most probably due to 4f–5d absorption bands of Ce^{3+}. However, in contrast to Eu^{2+}, this effect is significant only for emission in the deep red region of the emission band (λ_{em} = 770).

Photoluminescence decay kinetics

Photoluminescence decays were evaluated to get a better insight into the luminescence mechanism in Li_2MnCl_4:X (X = Eu^{2+}, Ce^{3+}).

Li_2MnCl_4. The PL decays of the broad band centred around 620 nm in undoped Li_2MnCl_4 were measured for different excitation wavelengths (λ_{ex} = 330, 370, 420, and 450 nm, see Fig. 10a). In all cases three exponential components were necessary for a satisfactory fit in the whole window (see Fig. S6, ESI†). However, the first component with a decay time

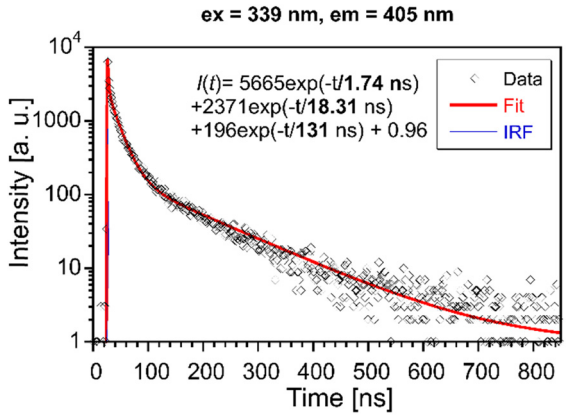

Fig. 9 PL decay curve of Li_2MnCl_4:Eu (λ_{ex} = 339 nm, λ_{em} = 405 nm). Red solid line is convolution of function $I(t)$ and instrumental response function IRF.

below the resolution of the measurement (1.334 μs per ch) originates from light scattering and is included only to achieve a satisfactory fit. Therefore, only two components correspond to Mn^{2+} luminescence. Fast (~70 μs) and slow (~300 μs) components are present for all four excitation wavelengths with over 90% contribution of the fast component (see Table S3, ESI†). The intensity-weighted mean decay times are 88.6, 87.5, 84.5, and 92.9 μs for excitation wavelengths of 330, 370, 420, and 450 nm respectively. Similar values of the mean decay time agree with the assumption that the emission band in the undoped Li_2MnCl_4 results from $^4T_{1g}$ (^4G) → $^6A_{1g}$ (^6S) for all four excitation wavelengths. However, a decay time of around 1 ms is expected for the $^4T_{1g}$ (^4G) → $^6A_{1g}$ (^6S) transition due to the violation of both parity and spin selection rules. The acceleration of the PL decay kinetics is most probably due to heavy concentration quenching which is expected when the luminescence centre is a matrix element. Such strong concentration quenching was reported by Song *et al.*[26] for heavily doped Mn^{2+} doped spinel. Furthermore, a strong quenching would explain the fairly low intensity of Mn^{2+} emission.

Li_2MnCl_4:Eu^{2+} and Li_2MnCl_4:Ce^{3+}. For Li_2MnCl_4:Eu^{2+} the PL decay kinetics were monitored at three different emission wavelengths (see Fig. 9 and 10b). At 405 nm corresponding to Eu^{2+} 5d → 4f emission and 670 nm and 770 nm corresponding to the maximum and long wavelength edge of the red emission band, respectively. The PL decay kinetics of the emission band is centred at 405 nm, which was ascribed to 5d → 4f emission of Eu^{2+}, was fitted using three exponential components (see Fig. 9).

The mean decay time is 53 ns. Such a value is much lower than expected (and reported for Eu^{2+} in chloride matrices[27–29]) for 5d → 4f emission of Eu^{2+} (~1 μs) due to partial violation of the spin selection rule. However, the acceleration of PL decay kinetics is consistent with the presence of energy transfer from Eu^{2+} to Mn^{2+}. The PL decay kinetics of the red emission band was monitored at 670 nm and 770 nm for both Eu^{2+} and Ce^{3+} doped samples (see Fig. 10). The excitation wavelengths were 340, 370, and 450 nm for Li_2MnCl_4:Eu (see Fig. 10b and Fig. S7,

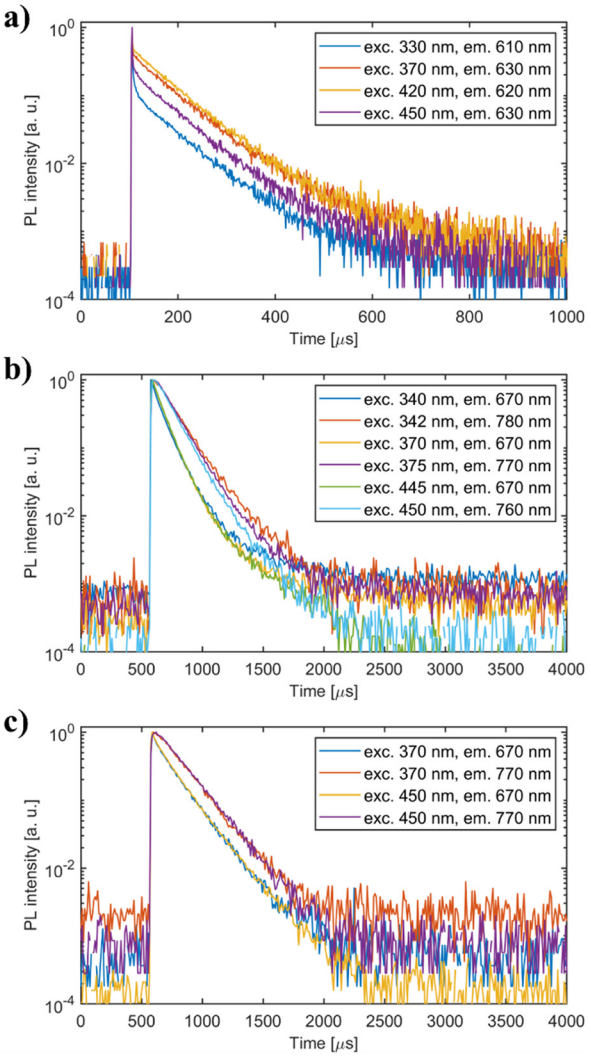

Fig. 10 PL decay curves of (a) undoped Li_2MnCl_4 (b) Li_2MnCl_4:Eu^{2+} and (c) Li_2MnCl_4:Ce^{3+}. Excitation and emission wavelengths are noted in the legend.

ESI†) and 370 and 450 for Li_2MnCl_4:Ce (see Fig. 10c and Fig. S8, ESI†). The results are summarized in Table 2. Generally, the PL decay times are longer for Ce doping. For both Eu and Ce doping the PL decay times are longer for emission at 770 nm compared to 670 nm. Moreover, the decay curves measured at 770 nm exhibit an observable rise time. This is a sign of a relatively slow (~μs) energy transfer towards the emission centre with lower energy of emission. The results suggest that the red emission band in doped Li_2MnCl_4 is composed of at least two components with different decay kinetics. The prolongation of the decay times is attributed to (i) an increase of emission lifetime with emission wavelength[30] and (ii) partial suppression of concentration quenching resulting from a larger Stokes shift.

Radioluminescence spectra

Similarly to the PL measurements, the RL emission of the doped samples exceeds the sensitive region of the used PMT.

Table 2 Mean PL decay times of Eu and Ce doped Li_2MnCl_4

	Mean decay time [μs]				
	Li_2MnCl_4:Eu			Li_2MnCl_4:Ce	
em\ex	340 nm	370 nm	450 nm	370 nm	450 nm
670 nm	129	131	115	172	171
770 nm	171	162	151	209	215

Therefore, the RL spectra were measured using both PMT and CCD-based photodetectors (see Fig. S9, ESI†). Fig. 11 depicts the RL spectra of all three samples in the range from 200 to 1100 nm together with the $Bi_4Ge_3O_{12}$ reference sample and commercially available Li glass neutron scintillator GS20. The spectra were constructed by "glueing" data from PMT (200–800 nm) and CCD (400–1100 nm). The RL peak amplitude of undoped Li_2MnCl_4 was used to calculate amplitude ratios of both RL spectra (measured with PMT and CCD) because it is well reproduced in both ranges. The RL spectrum of Li_2MnCl_4:Eu shows a low-intensity band centred at 405 nm (see Fig. 11 and Fig. S10, ESI†). The position coincides very well with the PL band of Eu^{2+} 5d → 4f emission. A very weak structured band centred at around 350 nm is observed in all three samples (see Fig. S10, ESI†). In the Ce doped sample it seems to be overlapped with a different broad band. This could be due to the 5d → 4f emission of Ce^{3+}. However, the extremely low intensity does not allow precise assignment of either of the bands. The RL efficiencies (integral of RL spectra) are 1.2, 6.6, and 12.2% of the BGO reference sample for undoped Li_2MnCl_4, Li_2MnCl_4:Eu, and Li_2MnCl_4:Ce respectively.

The RL spectra of all three samples were fitted assuming a Gaussian band shape (see Fig. S11–S13, ESI†). For undoped Li_2MnCl_4 the spectrum is well fitted using single Gaussian centred at 1.97 eV (629 nm). This is in agreement with the assumption of single emission pathway $^4T_{1g}$ (^4G) → $^6A_{1g}$ (^6S). On the other hand, two Gaussians were necessary for a satisfactory fit of RL spectra of Eu^{2+} and Ce^{3+} doped samples (see Fig. S12 and S13, ESI†). The centres of the Gaussians coincide very well for both Eu^{2+} (1.88 eV and 1.76 eV) and Ce^{3+} (1.88 eV and 1.74 eV) doped samples. However, their relative contribution differs significantly. For the Eu^{2+} doped sample, the contributions are 32.4% and 67.6% for 1.88 eV (660 nm) and 1.76 eV (705 nm) respectively. For the Ce^{3+}-doped sample, the contributions are 12.4% and 87.6% for 1.88 eV (660 nm) and 1.74 eV (713 nm) respectively. This would suggest that the nature of the luminescence centre is similar in both Eu^{2+} and Ce^{3+}-doped samples. However, in the Ce^{3+} doped sample, the lower energy centre is excited more efficiently.

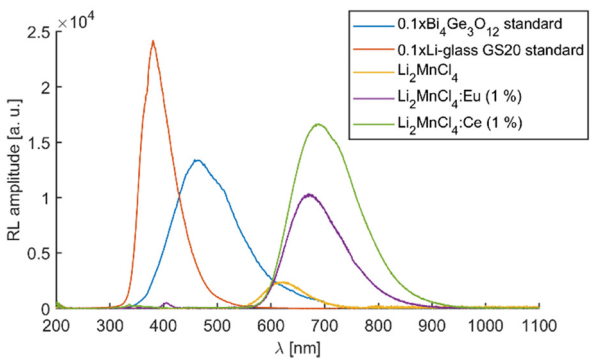

Fig. 11 RL spectra of all three Li_2MnCl_4 samples together with BGO and glass neutron scintillator GS20 reference samples. The amplitude of BGO and GS20 spectra was divided by 10 for better comparison.

Luminescence mechanism in doped samples

Based on the presented results we suggest a hypothesis explaining luminescence mechanisms in the Eu^{2+} and Ce^{3+} doped Li_2MnCl_4. The structure of Li_2MnCl_4 has two cationic crystallographic positions: tetrahedral one occupied by Li and octahedral one equally occupied by Li^+ and Mn^{2+} (see XRPD results above). Due to the large size of Eu^{2+} and Ce^{3+} cations, they should preferentially occupy the octahedral position. The crystal radius of Eu^{2+} (1.31 Å) and Ce^{3+} (1.15 Å) is 35 and 18% larger than Mn^{2+} (0.97 Å) in 6-coordination respectively. Therefore, the substitution of Eu^{2+} or Ce^{3+} for Mn^{2+} (possibly even octahedrally coordinated Li^+) results in the expansion of the substituted octahedra and consequentially compression of its neighbouring $MnCl_6$ octahedra. Such compression results in a redshift of the $^4T_{1g}$ (^4G) → $^6A_{1g}$ (^6S) emission due to a stronger crystal field experienced by Mn^{2+} (see Fig. 5). The emission from compressed $MnCl_6$ octahedra is less susceptible to concentration quenching due to larger Stokes shift. This effect could be further increased by the substitution of Cl^- with S^{2-} from the starting materials (EuS or Ce_2S_3). A higher negative charge of sulphur compared to chlorine increases the crystal field and therefore contributes to the redshift of the Mn^{2+} emission. Even though the segregation coefficient of sulphur should be very low it could incorporate into lattice as a charge compensation centre *i.e.* following charge compensated octahedra could be present in the Eu^{2+} or Ce^{3+} Li_2MnCl_4: $(Eu_{Li}Cl_5S)^{5-}$,$(Eu_{Mn}Cl_6)^{4-}$, $(Ce_{Li}Cl_4S_2)^{5-}$, and $(Ce_{Mn}Cl_5S)^{4-}$. If such a charge compensation effect occurs a higher concentration of S^{2-} is expected for Ce^{3+} doped samples. Of course, other charge-compensating defects like lithium vacancy or Cl^- interstitial could also occur in the doped samples. The proposed effect together with efficient energy transfer from Eu^{2+} and Ce^{3+} to Mn^{2+} would explain both redshift and increased intensity of Mn^{2+} emission in Eu^{2+} and Ce^{3+} doped Li_2MnCl_4. However, further study is necessary to confirm or disprove the incorporation of sulphur into Li_2MnCl_4.

Even though the PL decay kinetics of Mn^{2+} in Li_2MnCl_4 are too slow to be used as a scintillator in photon counting applications its emission matches very well an interval of 650–1000 nm which was identified by Matsukura *et al.*[5] as a target for emission of scintillation for long-distance dose monitoring. This technique is being developed to monitor the dose under harsh conditions, *e.g.* during the decommissioning of the Fukushima nuclear powerplant site. Li_2MnCl_4:Ce could be used in a similar system for real-time monitoring of neutron flux. Encapsulation of Li_2MnCl_4:Ce in a polymer with a high hydrogen content could serve three purposes at once: a protective casing to prevent air exposure, a neutron moderator, and a light guide to limit light losses. Moreover, low density (ρ = 2.4 g cm^{-3}) and effective atomic number (Z_{eff} = 17.1) of Li_2MnCl_4 will result in a

very low gamma detection efficiency, *i.e.*, a low gamma background. However, the feasibility of such a device would have to be tested in the high-intensity mixed neutron gamma field ideally using fully enriched ^{6}Li to maximize neutron detection efficiency.

Conclusions

We presented a novel red-emitting scintillator Li_2MnCl_4 which combines high Li content (28.5%$_{at}$), low density (ρ = 2.4 g cm^{-3}), and low effective atomic number (Z_{eff} = 17.1). This makes Li_2MnCl_4 a promising candidate for remote neutron flux monitoring with low gamma background. In particular, for measurements in high flux mixed neutron-gamma fields. The luminescence mechanism in undoped Li_2MnCl_4 was investigated in detail and all the absorption and emission bands were assigned according to the Tanabe–Sugano diagram. Doping with Eu^{2+} and Ce^{3+} was investigated to improve the scintillation performance. Doping with Eu^{2+} and Ce^{3+} resulted in a 5.5 and 10 times increase in radioluminescence efficiency respectively which points to the dopant-enhanced energy transfer towards the Mn sublattice in the scintillation mechanism taking into account that the increase of the photoluminescence mean decay time of Mn^{2+} is less than 2.5 in doped samples compared to the undoped one (Table 2 and Table S3, ESI†). However, even for the best sample the RL efficiency is only 12.2% of the $Bi_4Ge_3O_{12}$ reference sample which is presumably due to strong concentration quenching in the Mn-sublattice. The Mn^{2+} emission lifetime of about 21–22 ms[17] was measured in the $CaCl_2$ host at room temperature which is about 107× longer than the mean decay time measured for the Ce-doped Li_2MnCl_4 sample (Table 2). In the absence of concentration quenching, we could thus expect the integral efficiency of 107 × 12.2% > 1300% of BGO. Considering a typical BGO scintillation light yield of 8000 ph per MeV it provides an intrinsic light yield limit of LI_2MnCl_4-based material above 100 000 ph per MeV.

Based on the presented data we propose a luminescence mechanism in Eu^{2+} and Ce^{3+} doped Li_2MnCl_4 involving energy transfer from the dopants to Mn^{2+}, a local lattice distortion around the dopant and a possible charge compensation in case of the Ce^{3+} dopant. Distorted/perturbed Mn^{2+} sites near dopants show more red-shifted emission and lower susceptibility to concentration quenching. It consistently results in higher Mn^{2+} emission intensity in RL spectra and slower PL decay. Concentration quenching in the Mn^{2+} sublattice appears to be the main reason for the rather low scintillation efficiency of Li_2MnCl_4 -based materials in this study. Future work will be focused on diminishing this deteriorating process through the introduction of suitable near-infrared emitting dopants.

Author contributions

Vojtěch Vaněček – conceptualization, data curation, formal analysis, investigation, validation, visualization, writing – original draft, and writing – review & editing. Robert Král – conceptualization, funding acquisition, project administration, investigation, validation, supervision, and writing – review & editing. Kateřina Křehlíková – data curation, formal analysis, investigation, validation, visualization, and writing – review & editing. Kučerková Romana – data curation, formal analysis, investigation, and visualization. Vladimir Babin – data curation, formal analysis, investigation, and visualization. Petra Zemenová – data curation, formal analysis, and investigation. Jan Rohlíček – data curation, formal analysis, and investigation. Málková Zuzana – data curation, formal analysis, and investigation. Jurkovičová Terézia – data curation, formal analysis, and investigation. Martin Nikl – conceptualization, funding acquisition, project administration, supervision, and writing – review & editing.

Data availability

Data for this article are available at ''ASEP – Repository of the Czech Academy of Sciences'' at **https://doi.org/10.57680/asep.0587383**.

Conflicts of interest

There are no conflicts to declare.

Acknowledgements

The work is supported by the Operational Programme Johannes Amos Comenius financed by the European Structural and Investment Funds and the Czech Ministry of Education, Youth and Sports Project No. SENDISO - CZ.02.01.01/00/22_008/0004596. This work was supported by JSPS KAKENHI Grant Number K24KF00040. This research was conducted in the scope of the Japanese Society for Promotion of Science standard fellowship.

Notes and references

1 I. Stefanescu, M. Christensen, J. Fenske, R. Hall-Wilton, P. F. Henry, O. Kirstein, M. Müller, G. Nowak, D. Pooley, D. Raspino, N. Rhodes, J. Šaroun, J. Schefer, E. Schooneveld, J. Sykora and W. Schweika, *J. Instrum.*, 2017, **12**, P01019.
2 B. M. van der Ende, L. Li, D. Godin and B. Sur, *Nat. Commun.*, 2019, **10**, 1959.
3 R. T. Kouzes, A. T. Lintereur and E. R. Siciliano, *Nucl. Instrum. Methods Phys. Res., Sect. A*, 2015, **784**, 172–175.
4 R. G. Cooper, *Nucl. Instrum. Methods Phys. Res., Sect. A*, 2004, **529**, 394–398.
5 D. Matsukura, S. Kurosawa, C. Fujiwara, A. Yamaji, Y. Ohashi, Y. Yokota, K. Kamada, H. Sato, Y. Masao, T. Hanada, R. Murakami, T. Horiai, A. Yoshikawa, T. Takata and H. Tanaka, *J. Instrum.*, 2024, **19**, C02053.
6 K. Nitsch, A. Cihlář, Z. Málková, M. Rodová and M. Vaněček, *J. Cryst. Grow.*, 1993, **131**, 612–615.
7 K. Nitsch, M. Dušek, M. Nikl, K. Polák and M. Rodová, *Prog. Cryst. Growth Charact. Mater.*, 1995, **30**, 1–22.
8 V. Vanecek, R. Kral, J. Paterek, V. Babin, V. Jary, J. Hybler, S. Kodama, S. Kurosawa, Y. Yokota, A. Yoshikawa and M. Nikl, *J. Cryst. Grow.*, 2020, **533**, 125479.

9 *Flame Atomic Absorption Spectrometry Analytical methods*, Agilent Technologies, Inc., Printed in Australia, 8th edn, 2010.
10 H. D. Lutz and M. Schneider, *Z. Naturforsch. B*, 1990, **45**, 1543–1547.
11 R. Kanno, Y. Takeda and O. Yamamoto, *Mater. Res. Bull.*, 1981, **16**, 999–1005.
12 H. D. Lutz, W. Schmidt and H. Haeuseler, *J. Phys. Chem. Solids*, 1981, **42**, 287–289.
13 W. Schmidt and H. D. Lutz, *Ber. Bunsenges. Phys. Chem.*, 1984, **88**, 720–723.
14 M. M. E. Jacob, S. Rajendran, R. Gangadharan, M. S. Michael and S. R. S. Prabaharan, *Solid State Ionics*, 1996, **86–88**, 595–602.
15 H. D. Lutz, W. Schmidt and H. Haeuseler, *Z. Anorg. Allg. Chem.*, 1979, **453**, 121–126.
16 P. J. Alonso and R. Alcalá, *J. Lumin.*, 1981, **22** 321–333.
17 U. Caldiño G. and J. Rubio O., *Radiat. Eff. Defects Solids*, 1993, **127**, 83–91.
18 Tanabe-Sugano diagrams *via* spreadsheets, **https://wwwchem.uwimona.edu.jm/courses/Tanabe-Sugano/TSspread.html**, (accessed 14 June 2024).
19 R. Cao, Y. Rong, Y. Cao, B. Lan, C. Liao, J. Nie, F. Cheng and J. Wang, *Mater. Res. Bull.*, 2023, **166**, 112344.
20 G. K. B. Costa, S. S. Pedro, I. C. S. Carvalho and L. P. Sosman, *Opt. Mater.*, 2009, **31**, 1620–1627.
21 L. Qin, C. Chen, J. Wang, S. Bi, Y. Huang and H. J. Seo, *Mater. Res. Bull.*, 2019, **118**, 110494.
22 D. Castañeda, G. Muñoz H. and U. Caldiño, *Opt. Mater.*, 2005, **27**, 1456–1460.
23 P. Dorenbos, *J. Lumin.*, 2003, **104**, 239–260.
24 P. Dorenbos, *J. Phys.: Condens. Matter*, 2003, **15**, 575–594.
25 P. Dorenbos, *J. Lumin.*, 2013, **135**, 93–104.
26 E. Song, X. Jiang, Y. Zhou, Z. Lin, S. Ye, Z. Xia and Q. Zhang, *Adv. Opt. Mater.*, 2019, **7**, 1901105.
27 V. L. Cherginets, N. V. Rebrova, A. Y. Grippa, Y. N. Datsko, T. V. Ponomarenko, V. Y. Pedash, N. N. Kosinov, V. A. Tarasov, O. V. Zelenskaya, I. M. Zenya and A. V. Lopin, *Mater. Chem. Phys.*, 2014, **143**, 1296–1299.
28 M. Zhuravleva, B. Blalock, K. Yang, M. Koschan and C. L. Melcher, *J. Cryst. Grow.*, 2012, **352**, 115–119.
29 J. Selling, M. D. Birowosuto, P. Dorenbos and S. Schweizer, *J. Appl. Phys.*, 2007, **101**, 034901.
30 B. Di Bartolo, *Optical interactions in solids*, World Scientific Publishing Company, 2010.